https://doi.org/10.26599/FRICT.2026.9441249

Research Article

Electric current-induced tribological and microstructural degradation in bearing steel

Ganghui Jiang[1], Shuxin Li[1 *], Jibin Pu[2], Licheng Hua[1], Siyuan Lu[1]

[1] *School of Mechanical Engineering and Mechanics, Key Laboratory of Impact and Safety Engineering of MOE, Ningbo University, Ningbo 315211, China*

[2] *Key Laboratory of Advanced Marine Materials, Ningbo Institute of Materials Technology and Engineering, Chinese Academy of Sciences, Ningbo, 315201, China*

Corresponding author:

Prof. Shuxin Li

Tel.: +86 574 876009954;

Email: *lishuxin@nbu.edu.cn*

Received: April 22, 2025; Revised: February 12, 2026; Accepted: April 1, 2026

Abstract: The complex electrical environments inherent in electric vehicles often lead to premature failures of bearings. A comprehensive understanding of material behavior under current-carrying conditions is therefore essential. In this study, a current-carrying pin-on-disk tribometer was used to investigate the tribological response and microstructural degradation of bearing steel subjected to electric current. The results show that electric current significantly intensifies adhesive, oxidative, and abrasive wear, leading to increased coefficient of friction (COF) and wear volume. After 120 min of sliding, the average COF increases from 0.058 at 0 A to 0.066 at 1.5 A and 0.072 at 6 A, while the corresponding wear volumes at 1.5 A and 6 A are approximately 1.5 and 2 times that at 0 A, respectively. This deterioration is attributed to the combined effects of electro-thermal and athermal mechanisms.

Specifically, arc discharge in conjunction with frictional heating rapidly raises the surface temperature, inducing subsurface tempering and dynamic recrystallization. These thermally activated processes lead to microstructural softening, which in turn facilitates severe plastic deformation. Meanwhile, athermal effects accelerate dislocation motion and rearrangement, further affecting the material's mechanical properties.

Keywords: Bearing steel; Current-carrying tribology; Wear mechanism; Microstructural degradation.

1 Introduction

Bearings operate under complex electrical environments in applications such as electric vehicles, high-speed trains, and wind turbines [1]. For example, during motor operation, factors such as magnetic flux asymmetry, inverter-induced voltages, and triboelectric effects can subject bearings to both DC and AC electrical loads [2, 3]. The presence of electrical currents can lead to electrical erosion, frictional heat accumulation and lubrication degradation. This significantly raises the risks of adhesive and abrasive wear [4, 5]. Studies have shown that shaft currents can accelerate material degradation and significantly reduce bearing service life [6]. Although the mechanical performance of bearings has been extensively studied, their tribological behavior under current-carrying conditions remains insufficiently understood.

Compared to conventional sliding wear, current-carrying tribological behavior is more complex due to the coupled effects of mechanical and electrical wear [7]. Electrically induced damage can be categorized into frosting, fluting, pitting, spark tracks, and welding, based on surface morphology [8]. Song et al. [9] reported that when current density exceeds 0.95 A/mm^2, high-temperature discharges generate pits and induce martensite-to-ferrite transformation. Didenco et al. [10] observed erosion grooves caused by accumulated micro-discharges. At high voltages, lubricant film breakdown can produce pits, debris, and other erosion features. He et al. [3] demonstrated that electric current affects friction through surface melting, Joule heating, lubricant failure, and electrochemical corrosion. Cai et al. [11] found through combined experimental and data-driven analysis that current and load are the key factors affecting electrical contact performance. Arc discharge shifts the damage mechanism from mechanical to a compound mode, with ablation and oxidation intensifying over time and energy [12]. Similarly, Xue et al. [13] found that current application reduces the friction coefficient and wear of carbon film contacts, mainly due to the formation of carbon stacks with large wear particles and oxides in the wear region. However, most studies on current-carrying tribological behavior have primarily focused on macroscopic surface damage, with relatively few addressing subsurface microstructural evolution and the underlying damage mechanisms.

Besides, electric current can significantly influence the microstructure and mechanical properties of metals through both thermal and athermal effects [14]. Through current-induced thermal effects, it can promote diffusion-driven processes such as annealing [15], aging [16], and recrystallization [17]. Current can also interact with dislocations via electron wind, current constriction, and magnetic effects, thereby enhancing dislocation mobility and structural reorganization [18-20]. This facilitates deformation and accelerates microstructural evolution—a phenomenon known as electroplasticity [21, 22]. In tribological contacts, near-surface plastic deformation in bearing steel, together with the associated microstructural and mechanical evolution, can markedly affect tribological behavior. Accordingly, under current-carrying wear, electric current may degrade material performance through thermal effects and thus alter friction and wear. It may also promote dislocation motion and structural rearrangement via athermal interactions between electric current and dislocations, thereby influencing near-surface plastic strain accumulation and microstructural evolution and jointly affecting the tribological response. Nevertheless, systematic studies on how electric current affects tribological behavior through changes in material properties remain limited. In particular, athermal contributions in real contacts may couple with thermal effects, making temperature matching and decoupled validation challenging and warranting further investigation.

In this study, sliding wear tests were conducted on bearing steel using a pin-on-disk setup under oil-lubricated conditions, with varying current levels and wear times. The effects of electric current on tribological behavior, microstructural evolution, and mechanical properties were systematically examined. Emphasis was placed on subsurface microstructural changes and mechanical degradation during current-carrying wear, and their impact on frictional behavior. The findings offer valuable insights into bearing degradation and early failure in electric motor applications.

2 Experimental procedure

2.1 Materials

The raw material was AISI 52100 steel with the chemical composition (wt %): C, 0.91; Mn, 0.28; Cr, 1.51; Si, 0.21; S, 0.018; P, 0.025; Fe, balance. It was austenitized at 860 ℃ for 2 h, then oil-quenched to room temperature, and tempered at 160 ℃ for 1 h. The resulting microstructure consisted primarily of tempered martensite with finely dispersed carbides with an average diameter of approximately 0.8 μm, as shown in Fig. 1(a). According to the XRD results in Fig. 1(b), the matrix phase was mainly composed of martensite (α-Fe), residual austenite (γ-Fe, <5%), and M_3C cementite. The average matrix hardness was approximately 630 $HV_{0.025}$.

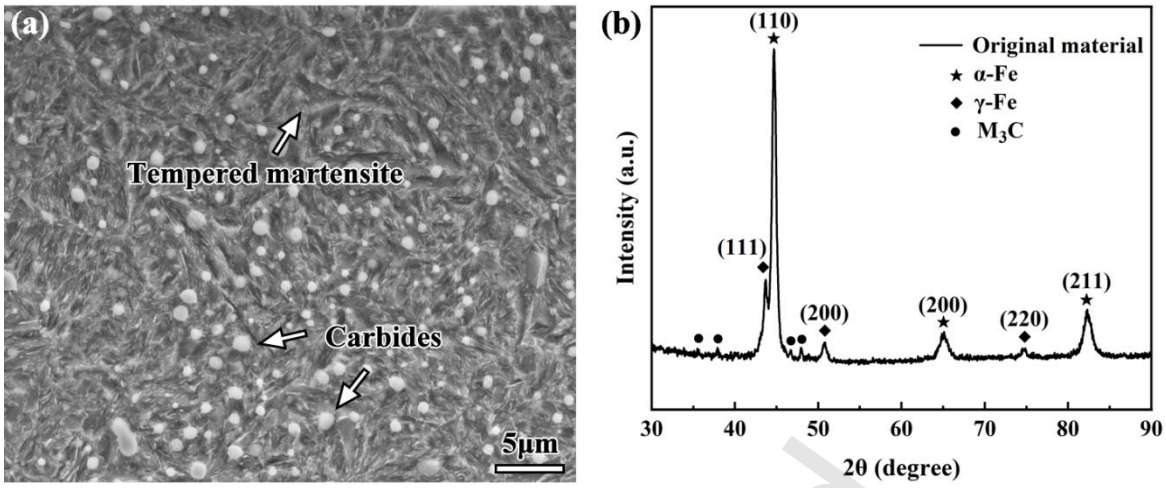

Fig. 1 (a) Microstructure of the original material; (b) XRD pattern of the original material.

2.2 Current-carrying sliding wear tests

Sliding wear tests were conducted using a modified MMU-2Z pin-on-disk tribometer equipped with an ANS®-JP20200D DC power supply, as shown in Fig. 2(a). DC was selected to partially simulate the electrical conditions in electric vehicle motors [4]. Both the disk and pin specimens were machined from AISI 52100 steel. The disks measured 99 mm in diameter and 8 mm in thickness, while the pins were 4.8 mm in diameter and 15.7 mm in length, with a hemispherical tip of 2.4 mm radius. All specimens were polished to achieve a surface roughness of 0.2-0.3 μm. Three pin specimens were mounted on the upper spindle fixture and rotated by a variable-frequency motor. The disk specimen was fixed to the lower spindle end, and axial loads were applied via a hydraulic system to establish contact and generate circumferential sliding. The power supply's positive and negative terminals were connected to the pin and disk fixtures, respectively, enabling current flow through the contact, as shown in Fig. 2(b) and 2(c). Tests were conducted at room temperature (23 ℃) with PAG gear oil lubrication (viscosity grade 68; kinematic viscosity 68.7 mm^2/s at 40 ℃; viscosity index 175).

The normal load and motor speed were set to 450 N and 200 rpm, corresponding to a relative sliding speed of 0.838 m/s. Current levels of 0, 1.5, and 6 A were selected based on typical stray currents (short-circuit characteristics) of 0.2-1.4 A observed in 1.5 kW induction motors [23]. The severity of bearing currents is commonly assessed by the nominal contact current density, $J = I/A_{HZ}$, where I is the applied current and A_{HZ} is the Hertzian contact area [24]. In the present three-pin configuration, I denotes the total circuit current and A_{HZ} denotes the total Hertzian contact area of the three pins ($A_{HZ,total}$). For the present geometry and loading, the Hertzian contact area per pin is $A_{HZ,per\ pin} \approx 0.055\ mm^2$, so $A_{HZ,total} = 3A_{HZ,per\ pin} \approx 0.165\ mm^2$, giving $J \approx 9$ and 36 A/mm^2 at 1.5 and 6 A, respectively. This J is a nominal average metric for comparing current levels rather than the instantaneous current density at an

individual pin. Based on prior studies [1, 9, 25], nominal contact current densities linked to pronounced bearing electrical damage range from a few tenths to the order of tens of A/mm^2, depending mainly on test operating conditions. Accordingly, 1.5 A falls within a typical damage-relevant range, whereas 6 A represents an accelerated condition with a higher current density. Wear times were 30, 60, and 120 min, with each test repeated three times to ensure repeatability.

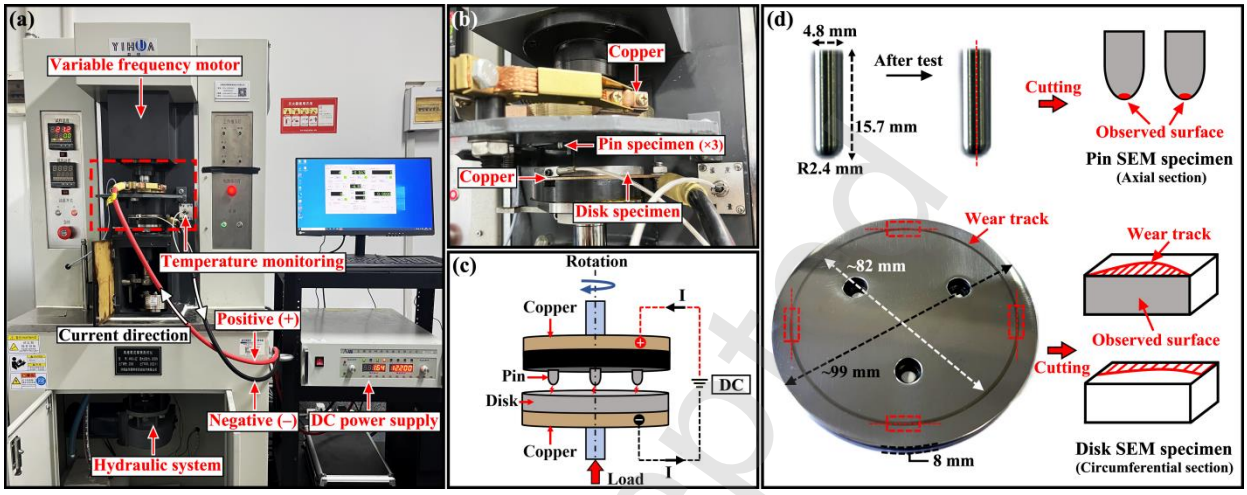

Fig. 2 (a) MMU-2Z current-carrying sliding wear test setup; (b) enlarged view of the boxed area in (a); (c) schematic diagram of the test system; (d) schematic illustration of sample preparation for SEM observation.

2.3 Microstructural characterization procedure

Macroscopic wear tracks morphology and profile were characterized using an OLYMPUS GX53 optical microscope (OM) and a Zeiss LSM 800 laser scanning confocal microscope (LSCM), respectively. Surface oxides were analyzed by a Renishaw inVia Reflex confocal Raman spectrometer with a scan range of 100-1000 cm^{-1}, excitation power of 1 mW, laser wavelength of 532 nm, and exposure time of 10 s. To examine subsurface microstructural changes, disk specimens were sectioned circumferentially and pin specimens axially, as shown in Fig. 2(d). The observation surfaces were mechanically ground and polished, then etched with 4% nitric acid in ethanol to reveal the microstructure. Subsurface microstructures were characterized using a SU-5000 scanning electron microscope (SEM) equipped with energy-dispersive X-ray spectroscopy (EDS) for elemental analysis. Phase analysis was performed using a Bruker D8 Advance X-ray diffractometer (XRD) with Cu Kα radiation (λ = 0.154 nm) at a scanning rate of 6°/min. Microhardness was measured using a YSMX automatic image-processing Vickers hardness tester under a 25 g load and 15 s dwell time.

3 Results

3.1 Coefficient of friction and wear volume

Fig. 3(a) shows the coefficient of friction (COF) over 120 min under different current levels. The wear process exhibits two distinct stages. Initially, the COF drops rapidly, stabilizes briefly, and then gradually rises across all conditions, with higher currents leading to consistently higher COF values. In the later stage, distinct behaviors are observed. At 0 A, the COF continues to decrease and stabilizes at 0.04, while 1.5 A and 6 A result in rising COFs, reaching 0.085 and 0.09, respectively. As summarized in Fig. 3(b), the average COF increases from 0.058 (0 A) to 0.066 (1.5 A) and 0.072 (6 A), indicating a clear current-dependent frictional response.

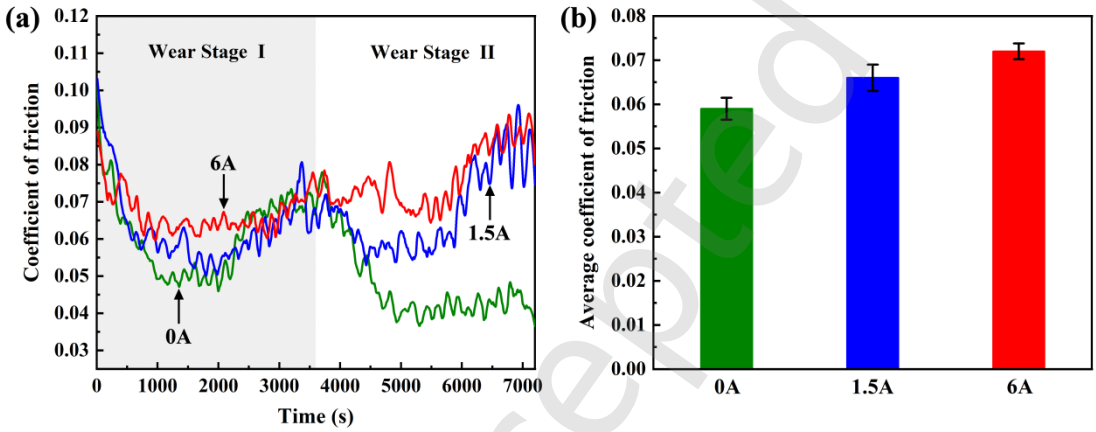

Fig. 3 (a) COF under different current levels during 120 min of wear; (b) average COF after 120 min of wear under different current levels.

Wear volume was determined by measuring the mass loss of pin specimens and estimating the worn geometry using the spherical cap model, accounting for the evolving contact from point to area due to the hemispherical tip. As shown in Fig. 4, wear volumes were comparable across all current levels at 30 min (155×10^6 μm^3). However, at 6 A, the wear volume increased markedly to 290×10^6 μm^3 at 60 min and 458×10^6 μm^3 at 120 min—approximately 1.2 and 2 times higher than those observed at 1.5 A and 0 A, respectively. These results indicate that electric current significantly accelerates material loss, particularly over prolonged sliding.

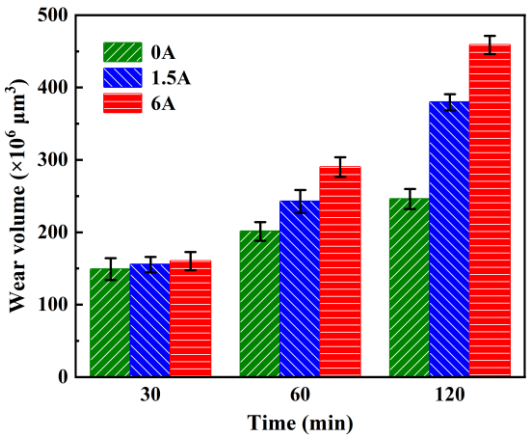

Fig. 4 Wear volume of pin specimens under different current levels and wear times.

3.2 The wear track surface analysis

Fig. 5 shows the macroscopic wear track morphologies on disk specimens under different conditions. Electric current significantly influenced surface morphology, with more severe damage observed at higher current levels for the same wear time. Black regions within the wear tracks, which were not oil residues due to post-test ultrasonic cleaning, were identified as tribo-films. At 6 A, tribo-films formed after 30 min and became denser, nearly covering the entire track by 120 min. A similar trend was observed at 1.5 A after 60 min. In contrast, under 0 A, tribo-films were sparse and confined to the central area, even after 120 min.

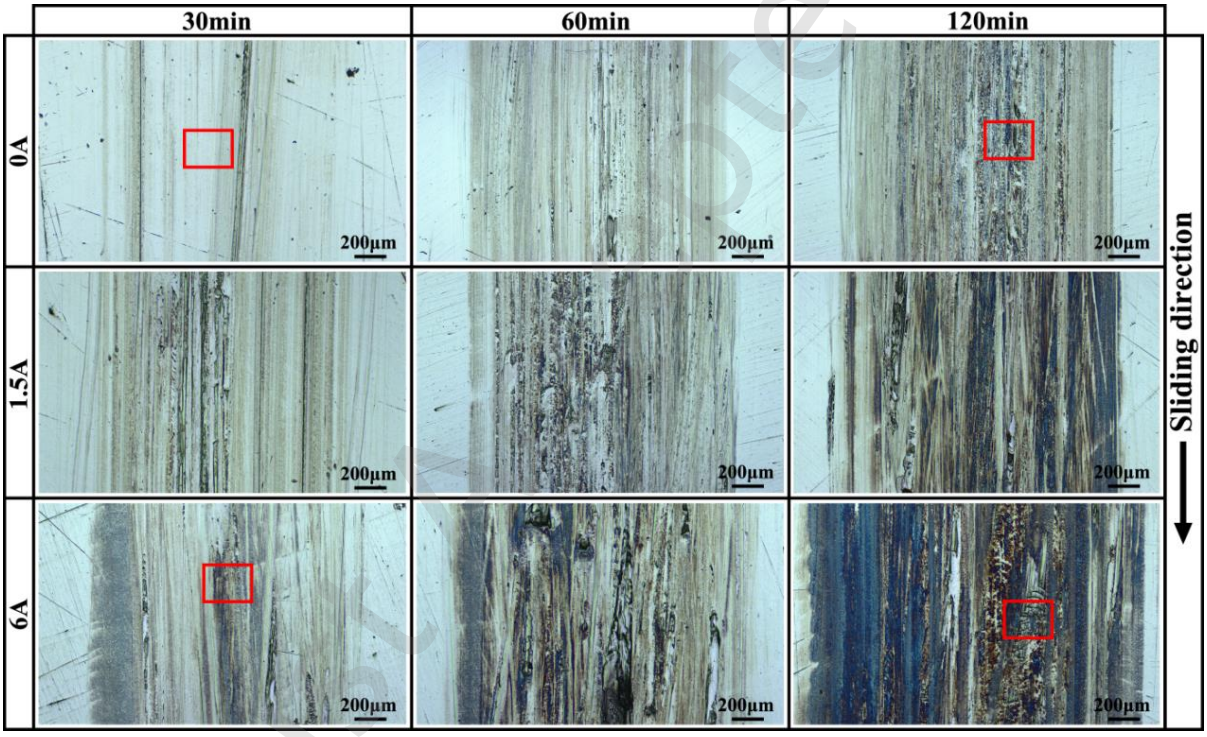

Fig. 5 OM images of wear track surfaces on disk specimens under various current levels and wear times.

To further investigate the wear behavior, Fig. 6 presents the microscopic morphologies of the central region of the wear tracks after 30 and 120 min of sliding at 0 A and 6 A, corresponding to the red-marked areas in Fig. 5. At 0 A after 30 min, the surface showed scratches and grooves parallel to the sliding direction, along with microcracks and slight delamination (Fig. 6(a)), indicating abrasive wear as the dominant mechanism. After 120 min, microcracks became more prominent, while delamination remained limited and the grooves appeared smoother (Fig. 6(b)), suggesting progressive plastic deformation during sliding. At 6 A after 30 min, in addition to scratches, grooves, and localized spalling, significant plastic deformation formed irregular bulges at the contact interface (Fig.

6(c)), typical of adhesive wear. After 120 min, both abrasive and adhesive wear intensified, with extensive delamination and spalling (Fig. 6(d)).

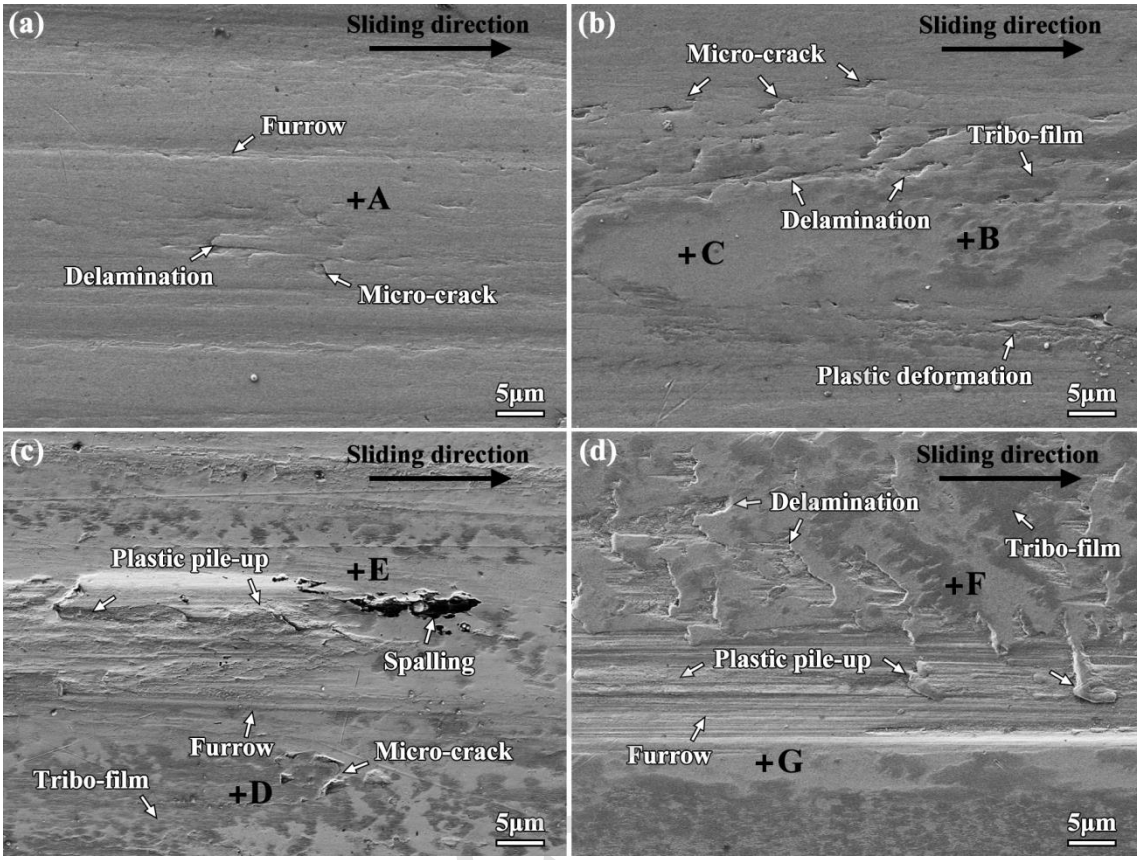

Fig. 6 SEM images of the central region of the wear tracks under different conditions: (a, b) 0 A for 30 and 120 min, respectively; (c, d) 6 A for 30 and 120 min, respectively.

To identify the composition of the tribo-film, EDS was performed on selected points within the wear track, as shown in Fig. 6 (marked in black). The results are summarized in Table 1. The black regions contain a higher oxygen content in addition to the substrate elements, indicating severe oxidation and the presence of oxide films. Combined with the macroscopic morphology in Fig. 5, these findings confirm that electric current promotes oxidative wear. SEM observations further reveal that the oxide film is unevenly distributed and locally damaged, suggesting it is prone to delamination under cyclic shear. This increases surface roughness and makes the underlying material more susceptible to damage.

Fig. 7 shows the cross-sectional profiles of wear tracks under different conditions. At the same wear time, track width increases with current. Compared to 0 A, current-carrying conditions exhibit more pronounced profile fluctuations and significantly higher pile-up, indicating enhanced plastic flow and material accumulation. After 120 min, the profile at 0 A becomes relatively smooth, while large undulations persist under current. These results are

consistent with the surface morphologies observed in Figs. 5 and 6.

Table 1 Major chemical compositions (wt%) of the marked regions shown in Fig. 6.

	O	C	Cr	Fe
A	0.52	5.12	1.48	92.88
B	17.07	5.93	1.57	76.43
C	1.86	5.09	1.23	91.82
D	16.93	5.61	1.36	76.10
E	1.91	5.84	1.46	90.79
F	17.75	5.89	1.24	75.12
G	0.97	5.15	1.35	92.53

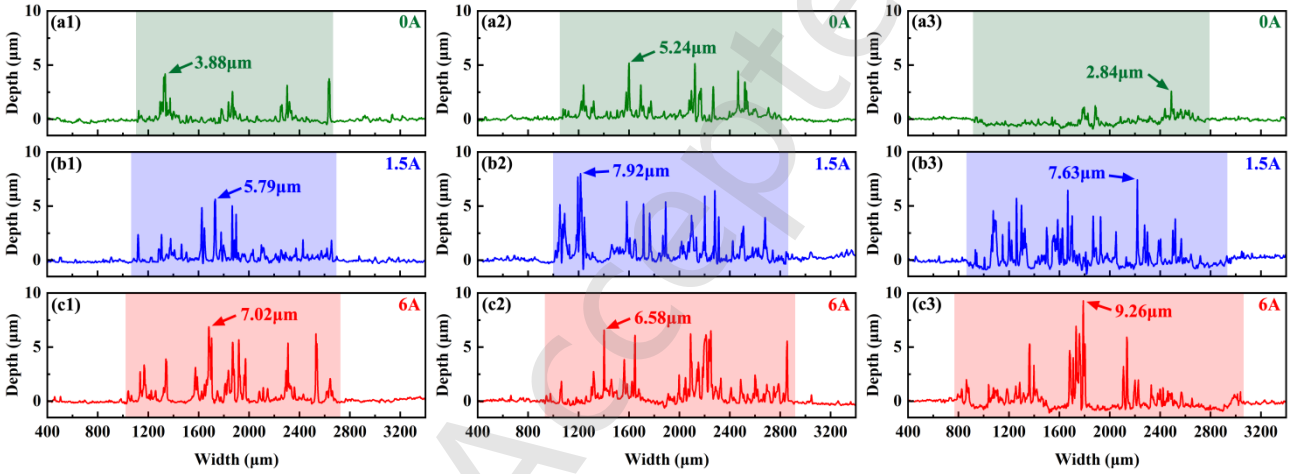

Fig. 7 Cross-sectional profiles of wear tracks under different current levels and wear times: (a1, b1, c1) after 30 min of wear; (a2, b2, c2) after 60 min of wear; (a3, b3, c3) after 120 min of wear.

3.3 The wear track cross-section analysis

The microstructural evolution during wear significantly influences tribological behavior. Fig. 8 presents SEM images of cross-sectional microstructures under different conditions. Sliding wear results in subsurface strain accumulation and the formation of a plastically deformed layer (PDL), where martensitic structures undergo flow deformation, distinct from the original tempered microstructure in Fig. 1(a). Compared to conventional wear, current-carrying conditions increase PDL thickness and induce more pronounced morphological changes. After 30 min, all samples exhibit elongated and bent martensitic structures inclined toward the surface, with greater curvature at 6 A. After 60 min, a gradient structure is observed at 6 A, including a severely plastically deformed layer (SPDL) within approximately 3 μm of the surface, contrasting with the other conditions. After 120 min, the PDL under 0 A remains dominated by elongated structures, while a gradient forms under 1.5 A. At 6 A, the SPDL becomes denser,

with deformation features barely discernible. These results indicate that electric current accelerates plastic deformation during wear, altering the material's mechanical properties. This accelerates surface damage and increases the likelihood of microcrack initiation (as indicated by black arrows), thereby raising the risk of pitting and spalling.

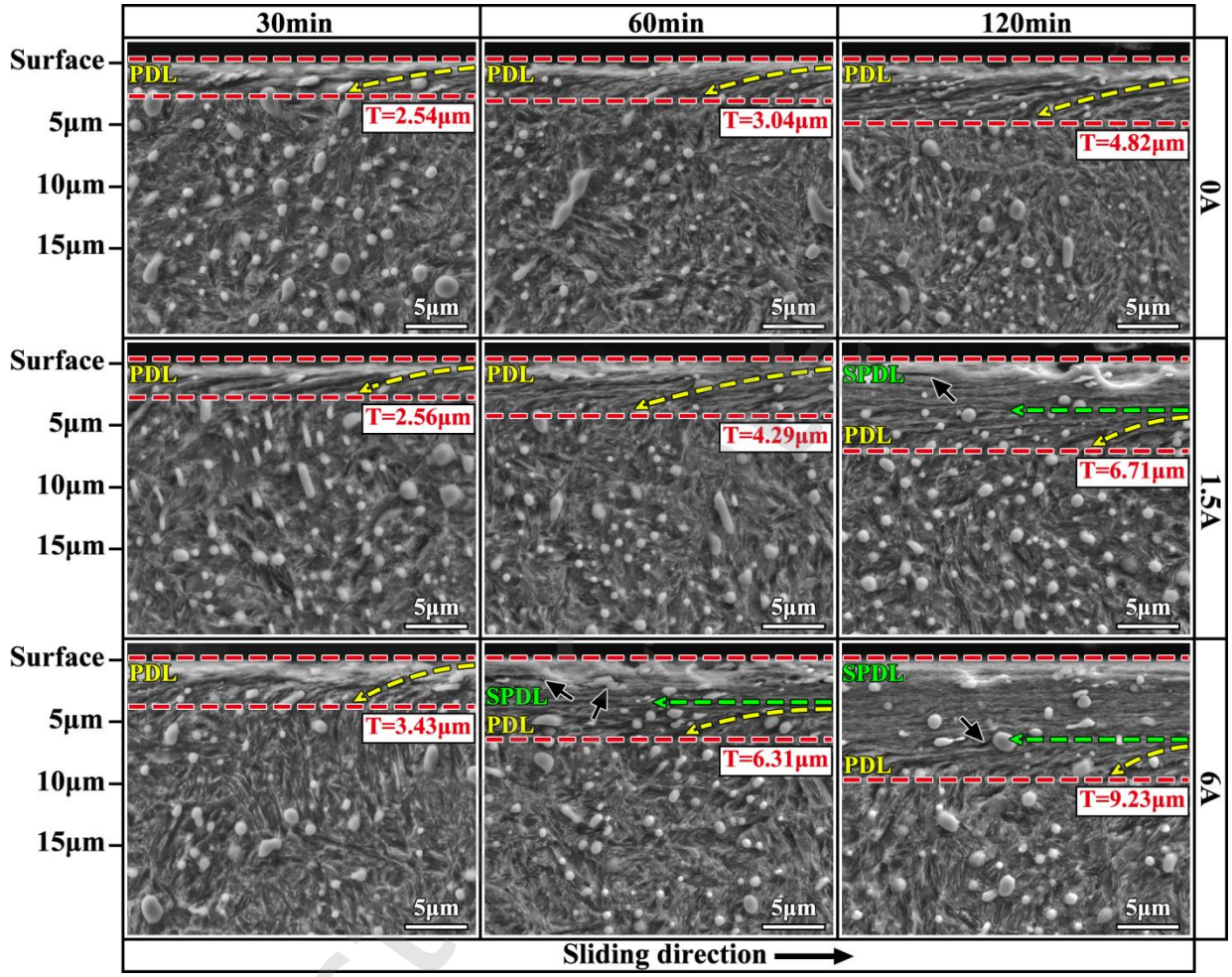

Fig. 8 Cross-sectional SEM images of wear tracks under different current levels and wear times.

4 Discussion

4.1 Estimation of temperature rise during current-carrying sliding wear

In sliding wear, frictional heating is inevitable. Under current-carrying conditions, additional Joule and arc heating further increase the interface temperature by combining with frictional heat [26, 27]. Temperature evolution was monitored using a built-in probe located 2 mm below the wear track, and the results are shown in Fig. 9. During the first 30 min, the temperature increased rapidly, then the rate of rise gradually slowed. Throughout the test, temperatures under current-carrying conditions remained higher than those without current. By the end, disk temperatures reached approximately 48 ℃, 53 ℃, and 60 ℃ under 0 A, 1.5 A, and 6 A, respectively. However, such

a small temperature difference is unlikely to significantly affect the tribological behavior. Considering heat dissipation through wear debris, plastic deformation, and bulk heat conduction within the specimen [28, 29], the actual temperature at the contact interface may be considerably higher than measured. Therefore, the temperature was estimated based on experimental observations and thermal models, providing a reasonable approximation despite the challenges in accurately determining it due to the complexity of frictional processes.

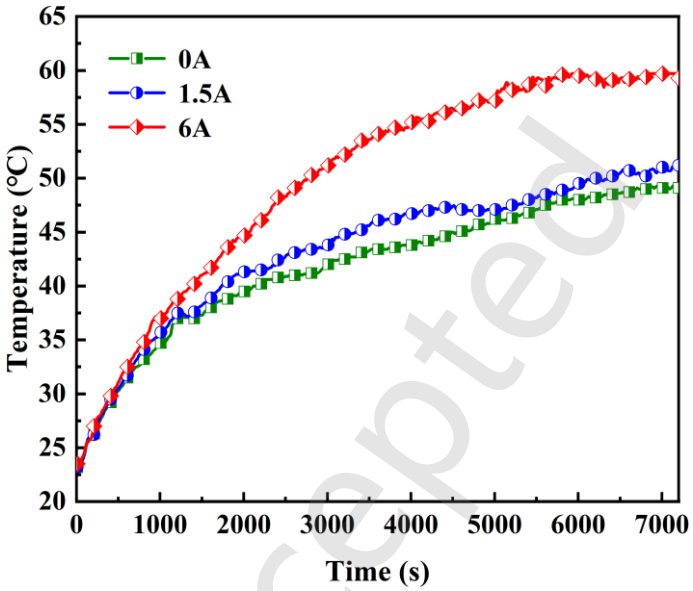

Fig. 9 Temperature evolution of the disk specimen during 120 min of wear under different current levels.

Frictional heating under no-current conditions was estimated using a one-dimensional transient heat conduction model, suitable for pin-on-disk contact [30]. The model assumes heat is generated at the contact interface, conducted into the material, and partially dissipated through surface convection. The local surface temperature is given by [31]:

$$T = \frac{Q_A}{h_s}\left\{1 - \mathrm{erfc}\left[h_s\sqrt{\frac{t}{K\rho c}}\right]\cdot\exp\left[\frac{h_s^2 t}{K\rho c}\right]\right\} \quad (1)$$

where h_s is the convective heat transfer coefficient, t is time, and ρ, c, and K are the material's density, specific heat, and thermal conductivity, respectively. The unit-area frictional heat flux Q_A is calculated as $Q_A = \mu Pv/A_s$, where μ is the COF (average value used), P is the normal load, v is the sliding velocity, and A_s is the wear track area, estimated from the cross-sectional profiles in Fig. 7. Parameter values are listed in Table 2. It should be noted that this model considers only one dimensional heat conduction and does not explicitly account for heat removal by the lubricant or the influence of wear debris accumulation on the heat source distribution and thermal boundary conditions. Moreover, by neglecting the approach to thermal steady state, it predicts a gradual temperature increase with time.

As a result, the interfacial temperature rise may be overestimated, but the prediction can serve as an upper bound estimate. Based on the data in Table 2, the predicted local frictional temperature under 0 A after 120 min is approximately 258 ℃.

Table 2 Parameters and values used in the calculation of temperature.

Parameter	Value
Convection heat transfer coefficient, h_s ($W \cdot m^{-2} \cdot K^{-1}$)	50
Specific heat, c ($N \cdot mm^{-2} \cdot K^{-1}$)	4.5
Density, ρ (kg/m^3)	7687
Thermal conductivity, K ($N \cdot s^{-1} \cdot K^{-1}$)	60
COF, μ	0.058
Normal load, P (N)	450
Sliding velocity, v (m/s)	0.838
Surface area, A_s (mm^2)	452.9
Specific heat capacity, C_p (J/(kg·K))	460
Effective resistance, R_e (μΩ·m)	1.2

When current flows through a metal, electrons accelerated by the electric field scatter with the lattice, increasing lattice vibrations and releasing heat as Joule heating [32]. In bearing steel, microstructural defects such as dislocations and grain boundaries, along with the lower conductivity of carbides compared to the martensitic matrix, can contribute to localized Joule heating [33]. However, after heat treatment, carbides are uniformly distributed (Fig. 1(a)), and the material's high thermal conductivity promotes efficient heat dissipation, minimizing local temperature gradients. The overall temperature rise due to Joule heating can be estimated by $\Delta T = Q/mC_p$, where m and C_p are the mass and specific heat capacity, respectively [32]. Joule heat Q is calculated as $Q = I^2R_et$, where I, R_e, and t represent current, effective resistance, and duration of current application. Parameter values are listed in Table 2. Assuming adiabatic conditions, the model gives an upper-limit estimate. Even at 6 A, the predicted temperature rise after 120 min is only 5.8×10^{-4} ℃ for the disk and 11.7 ℃ for the pin. The higher resistance of the pin, due to its smaller cross-sectional area, leads to greater heat accumulation. Nonetheless, the overall temperature rise remains low. A previous study reported a 7 ℃ increase in the outer ring of bearings after 120 min at 10 V (greater than the 1.5 V used at 6 A in this study), mainly attributed to Joule heating [9]. Therefore, under the present conditions, the thermal effect of Joule heating is considered negligible.

During current-carrying wear, the temperature rise in the wear track is primarily caused by arc heating. Current flow across the contact interface may intensify the local electric field, and momentary contact interruptions due to friction or material detachment can exceed the breakdown threshold, triggering arc discharges with transient high

temperatures and intense thermal shock [34, 35]. Fig. 10 shows typical arc-induced damage. Electrical erosion appears as randomly distributed black spots consisting of fine particles enriched in carbon, oxygen, and chromium (Fig. 10(a)). Most erosion pits are circular, with clear evidence of melting and oxidative ablation (Fig. 10(b)). In more severe cases, extensive melting and burning are observed, with severe oxidation and numerous cracks in the burned regions (Fig. 10(c)). These arc burns are mainly found under 6 A and tend to concentrate in scratches and ploughing grooves. Higher current and surface irregularities enhance local electric fields, increasing arc discharge probability [36]. The damage consistently shows oxidation and melting, indicating local temperatures exceeding the melting point of steel (approximately 1500 ℃ [37]). Arc discharge is considered adiabatic, with instantaneous temperatures reaching up to 10,000 K [38]. Such extreme temperatures generate localized heat-affected zones, leading to material softening and spalling caused by thermal stress, which in turn promotes further arc activity. Although local temperatures spike briefly, the short duration and random nature of arc events allow rapid heat dissipation, keeping the overall wear track temperature relatively low [12, 39].

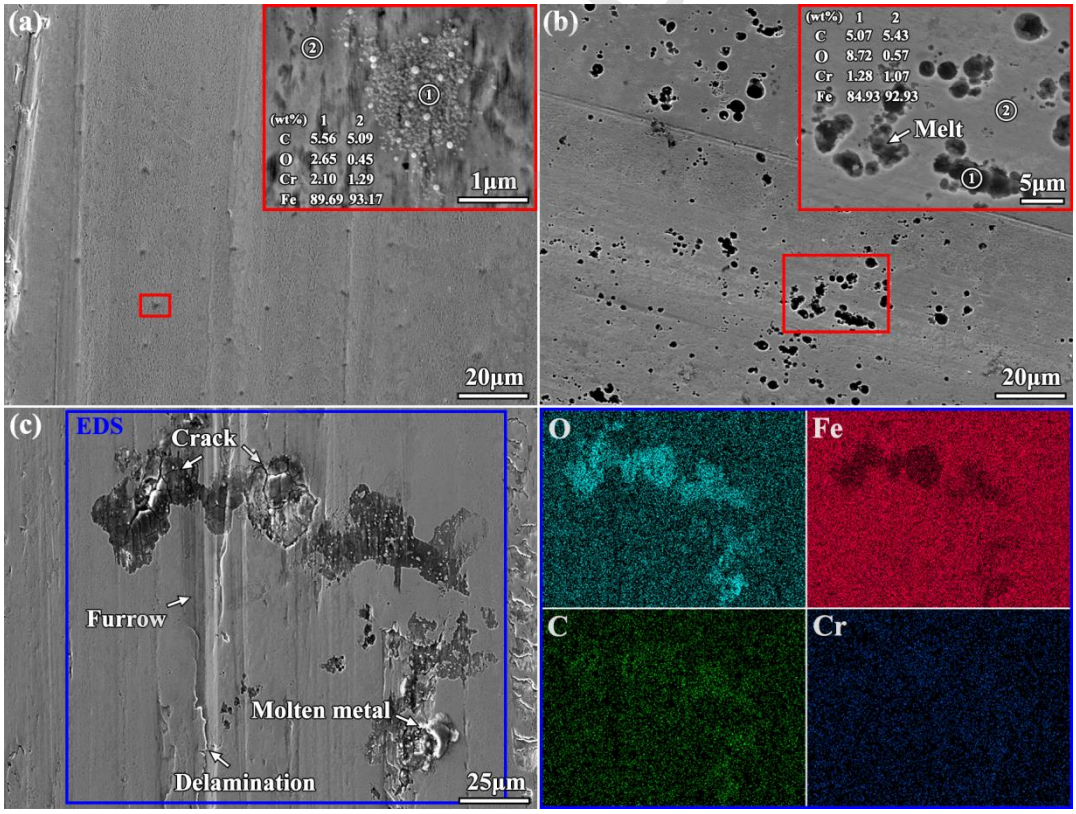

Fig. 10 Typical morphologies of electrical erosion damage within the wear track under current-carrying conditions: (a) electrical erosion marks and corresponding magnified view; (b) erosion pits and corresponding magnified view; (c) arc discharge burns and localized EDS analysis.

The actual wear temperature can be inferred from the analysis of wear products. Fig. 11 shows Raman spectra

obtained from the central region of the wear track under different conditions. The main wear products are Fe_2O_3 and Fe_3O_4. Characteristic Raman peaks for Fe_2O_3 appear at 229cm^{-1}, 299cm^{-1}, 410cm^{-1} and 670cm^{-1} [40], while those for Fe_3O_4 are observed at 300cm^{-1}, 530cm^{-1} and 670cm^{-1} [41]. Under 0 A and 1.5 A, only Fe_2O_3 was detected after 120 and 60 min, respectively. In contrast, under 6 A, Fe_2O_3 appeared as early as 30 min, and Fe_3O_4 was detected after 60 min. A similar phenomenon was reported in [40]. This variation is primarily attributed to temperature differences, as Fe_2O_3 typically forms around 300 ℃ [42, 43], while Fe_3O_4 forms at higher temperatures between 450 ℃ and 600 ℃ [44, 45]. Under 0 A, the presence of Fe_2O_3 after 120 min suggests a temperature of approximately 300 ℃, aligning with the value predicted by Eq. (1). Accordingly, the temperatures at 30 and 60 min are estimated at about 115 ℃ and 171 ℃, respectively. Under 6 A, the temperature reached 300 ℃ after 30 min, and the presence of Fe_3O_4 at 60 min suggests it exceeded 450 ℃. Conservatively, the overall wear track temperature after 120 min is estimated at 600 ℃, while local regions affected by arc discharge may be significantly higher. At 1.5 A, the temperature evolution lies between the 0 A and 6 A conditions, starting similarly to 0 A but rising more rapidly due to increased arc activity over time.

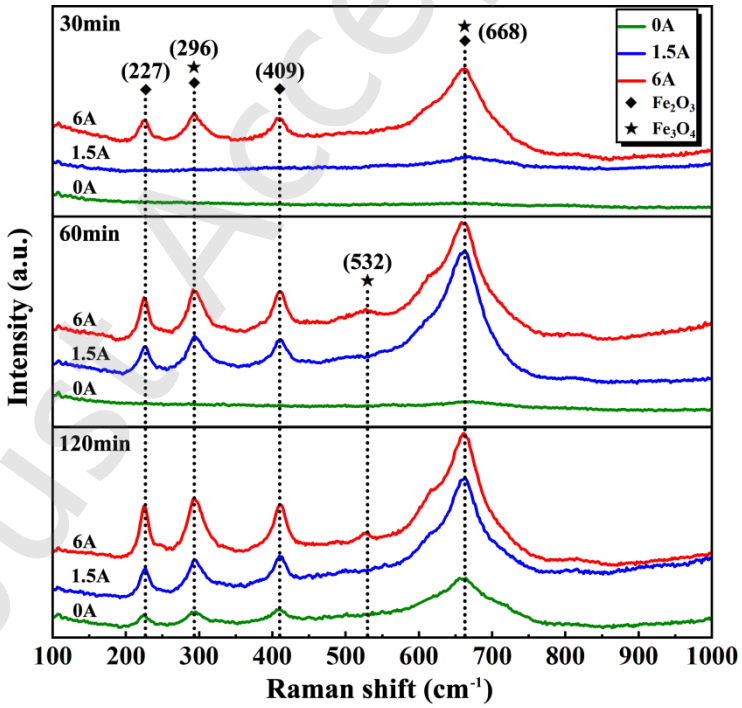

Fig. 11 Raman spectra of the wear track under different current levels and wear times.

4.2 Effect of electric current on tribological behavior

As shown in Figs. 3 and 4, electric current increases COF and wear volumes, indicating deteriorated tribological performance. These changes are closely linked to a shift in wear mechanisms under current-carrying conditions. According to Figs. 5-7, abrasive wear dominates under no-current conditions, with minor oxidative wear

developing over time. In contrast, current-carrying conditions induce significant abrasive, adhesive, and oxidative wear from the early stages, which intensify with higher current and longer wear time. Adhesive and oxidative wear are typically associated with elevated temperatures. The additional thermal effect from current is the main driving factor. Higher temperatures soften the interfacial material, enhance metallic bonding, and promote micro-welding between asperities. They also accelerate atomic diffusion, facilitating oxide film formation. For most metals, oxidation kinetics follow the relation [46]:

$$h = Ct^{\frac{1}{2}} \tag{2}$$

where h, C and t represent the oxide film thickness, growth rate, and oxidation time. The film growth rate is highly temperature-dependent and can be expressed as [47]:

$$K = A\exp(-\frac{Q}{RT}) \tag{3}$$

where K is the rate constant, A is the pre-exponential factor, Q is the activation energy, R is the gas constant, and T is the absolute temperature. According to these equations, the thickness and coverage of the oxide film increase with temperature and time. This further indicates that oxide films form more readily under current-carrying conditions, with greater thickness and coverage.

Oxide films generally inhibit adhesion and provide self-lubricating effects. Spikes et al. [5] reported that improved tribological performance under current-carrying conditions is related to current-induced ionic adsorption of additives or oil molecules, which accelerates oxide formation. Farfan-Cabrera et al. [6, 23] also found that applying direct current reduced the friction coefficient in bearing and gear steels due to rapid formation of oxide-based tribo-films. However, such effects were not observed in this study. Instead, oxide films appeared to aggravate wear. After 60 min of current-carrying wear, a relatively continuous oxide film had formed, yet the COF increased further and adhesive wear remained severe (Figs. 3-7). In fact, thick oxide films may spall from the surface, and arc erosion can further promote their fracture, generating oxide debris [48]. The competition between film spalling and regeneration largely determines the tribological behavior. EDS (Table 1) and Raman spectra (Fig. 11) indicate the oxide films primarily consist of Fe_2O_3 and Fe_3O_4. Compared to Fe_3O_4, Fe_2O_3 has a looser structure with lower load-bearing capacity and adhesion, making it more prone to cracking and detachment [49]. Although the hardness of Fe_2O_3 debris (2.7-8.3 GPa) is lower than that of AISI 52100 steel (~8.4 GPa) [6], accumulated debris can act as a third body, promoting oxidative and abrasive wear. Simultaneously, film removal exposes fresh, reactive metal surfaces that promote adhesion or rapid reoxidation. This cycle of film breakdown and regeneration degrades surface integrity and leads to shallow spalling (Figs. 6(c) and 6(d)).

Beyond the electro-thermal effects discussed above, current-carrying contact is also accompanied by an electric field, which may further influence tribological behavior by modifying lubrication and interfacial mechanics. Previous studies have shown that electric fields can drive electromigration of polar species and ions in lubricants and promote electrochemical reactions, thereby accelerating lubricant oxidative degradation [50, 51]. In addition, electric-field-induced electrostatic pressure and electrowetting may alter lubricant spreading and interfacial tension, reducing film stability and promoting a transition toward boundary lubrication, which can aggravate adhesion and electrical erosion [52, 53]. Furthermore, Xie et al. [54] reported that electric fields can induce microbubbles in confined liquid films, whose formation and collapse may locally disturb the film and aggravate electrical erosion. Electric fields may further enhance electrostatic attraction between asperities and thus increase friction [55].

In the present tests, the current source indicated output voltages of approximately 0.8 V at 1.5 A and 1.5 V at 6 A, implying a finite potential difference across the pin-disk electrical loop (including the contact region) and suggesting possible electric-field effects during current-carrying wear. Nevertheless, due to the lack of in situ characterization, the magnitude of the interfacial electric field and its coupling with film formation could not be quantitatively assessed. Based on prior studies, electric-field-related effects may act in conjunction with electro-thermal effects, contributing to lubrication deterioration, increased wear, and an increased risk of electrical erosion.

Based on the above analysis, the COF variations in Fig. 2 can be explained as follows. In the first stage, frictional and electrical heating under current-carrying conditions induce oxidative and adhesive wear. However, during the run-in period, extensive debris generation makes abrasive wear dominant, hindering oxide film formation and producing oxide particles that aggravate wear. As a result, COF trends are similar across all conditions but slightly higher under current-carrying ones. In the second stage, the contact surface stabilizes. Under no-current conditions, abrasive wear decreases and mild oxidative wear occurs locally due to limited heat. In contrast, sustained high temperatures under current-carrying conditions lead to dominant oxidative wear. At 1.5 A, an Fe_2O_3-rich oxide film gradually forms, but its loose structure and weak adhesion result in repeated spalling, promoting abrasive and adhesive wear and increasing COF. A similar effect occurs at 6 A. After 60 min, Fe_3O_4 formation promotes a more continuous oxide film, but excessive thickness reduces lubricant film effectiveness, increases arc discharge risk [56], and further accelerates wear and friction. In addition, the interfacial electric field under current-carrying conditions may also act together with electro-thermal effects to promote lubrication degradation, thereby influencing the COF.

4.3 Thermal effects of electric current on the mechanical properties of bearing steel

Under current-carrying conditions, the subsurface PDL exhibits greater thickness and altered morphology

compared to conventional wear, primarily due to shear strain gradients during sliding. Shear strain can be estimated from the displacement of flow-deformed structures within the PDL [57]. The depth dependence of displacement field can be represented by $y(x) = y_s\exp(-ks)$, where x and y_s denote the depth and surface displacement, respectively, in the X-O-Y coordinate system. For consistency, the origin was set at the midpoint of each cross-section (Fig. 8), as illustrated in Fig. 12(a). Detailed calculation procedures can be found in [58]. Fig. 12(b) shows the subsurface equivalent shear strain distributions after 30 and 120 min under different currents. Strain decreases exponentially with depth. Current-carrying conditions result in higher shear strain and deeper affected zones than the no-current case, with differences increasing over time. After 120 min, the maximum strain at 6 A reaches 92, which is 1.3 and 2 times higher than the values at 1.5 A and 0 A, respectively. Strain levels in plastic deformation processes are typically reported to range from 10 to 100 [59].

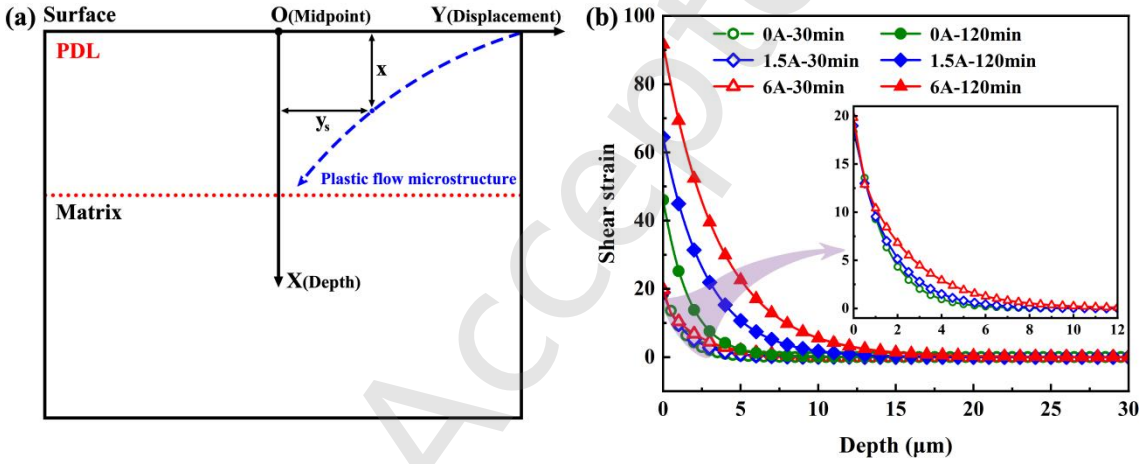

Fig. 12 (a) Schematic illustration of subsurface shear strain estimation; (b) shear strain variation with depth.

Sliding wear is essentially a fatigue loading process [60]. Subsurface plastic shear strain in metals is closely associated with friction-induced softening, which is further intensified by electro-thermal effects under current-carrying conditions. Prolonged high temperatures may also induce microstructural changes and reduce mechanical strength. To evaluate this, microhardness was measured at 10 μm intervals along the wear track depth under different conditions, as shown in Fig. 13. All samples exhibited a subsurface hardness gradient, with the highest hardness at the surface decreasing with depth. Compared to the no-current case, both surface and subsurface hardness changed notably under current. Surface hardness is influenced by multiple factors (to be discussed later), while subsurface hardness, less affected by shear strain, more directly reflects thermal effects of electric current. It decreased progressively with increasing current and wear time. After 120 min, subsurface hardness was about 630 $HV_{0.025}$ at 0 A, but dropped to 612 $HV_{0.025}$ and 600 $HV_{0.025}$ at 1.5 A and 6 A, respectively. Similar trends have been reported in

studies on hard turning [61] and rolling contact fatigue [9] of bearing steel under various current conditions.

Joule heating and arc discharge can transfer heat deeper into the material, enlarging the heat-affected zone beyond that caused by friction alone [1]. Martensite in this region may undergo tempering-like transformations. To verify this, carbide number and size within 50 μm of the surface were measured for the original material and samples worn under 0 A and 6 A for 120 min, as shown in Fig. 14. At 6 A, an increase in carbide number and size suggests high-temperature tempering (>300 ℃) occurred in this region. Supersaturated carbon precipitated from the martensitic matrix, forming carbides and reducing hardness. This weakened resistance to plastic deformation, allowing shear to penetrate deeper and increasing both the depth and severity of deformation. In contrast, under 0 A, the lower frictional temperature (258 ℃) may have triggered mild tempering, but no significant microstructural or hardness changes were observed. Notably, the tempering effect was confined to the near-surface region, with no evident changes in deeper regions.

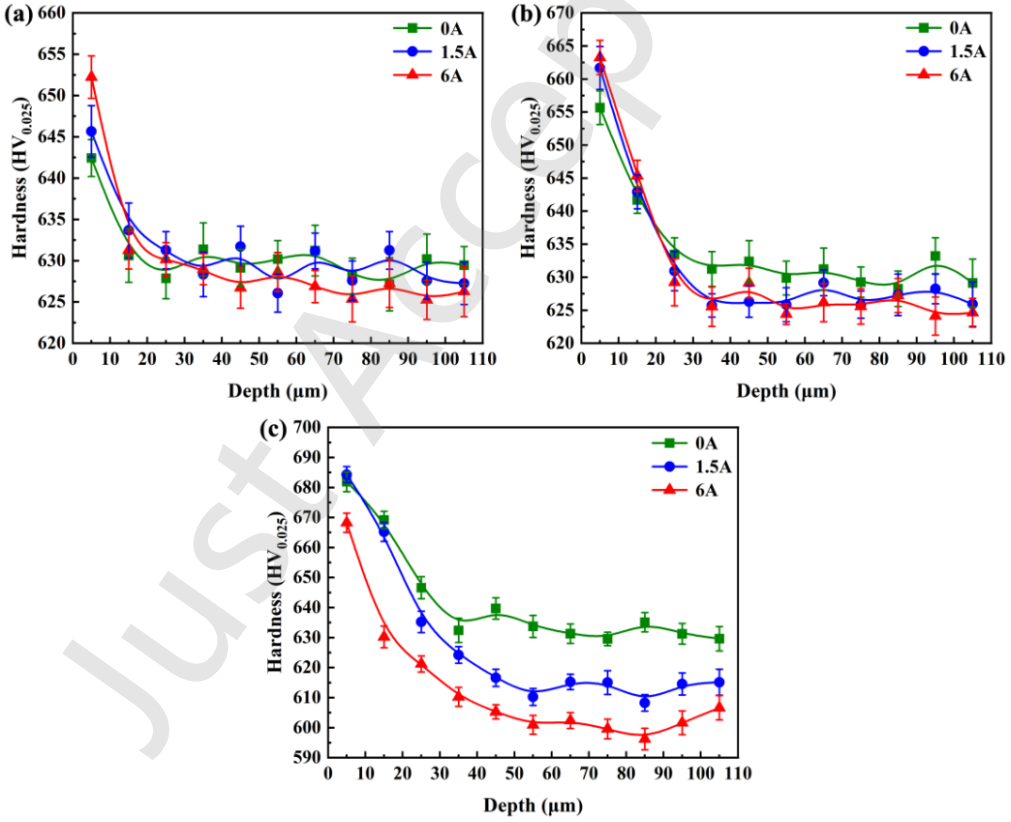

Fig. 13 Microhardness profiles along the cross-section of the wear track under different wear times and current levels: (a) after 30 min of wear; (b) after 60 min of wear; (c) after 120 min of wear.

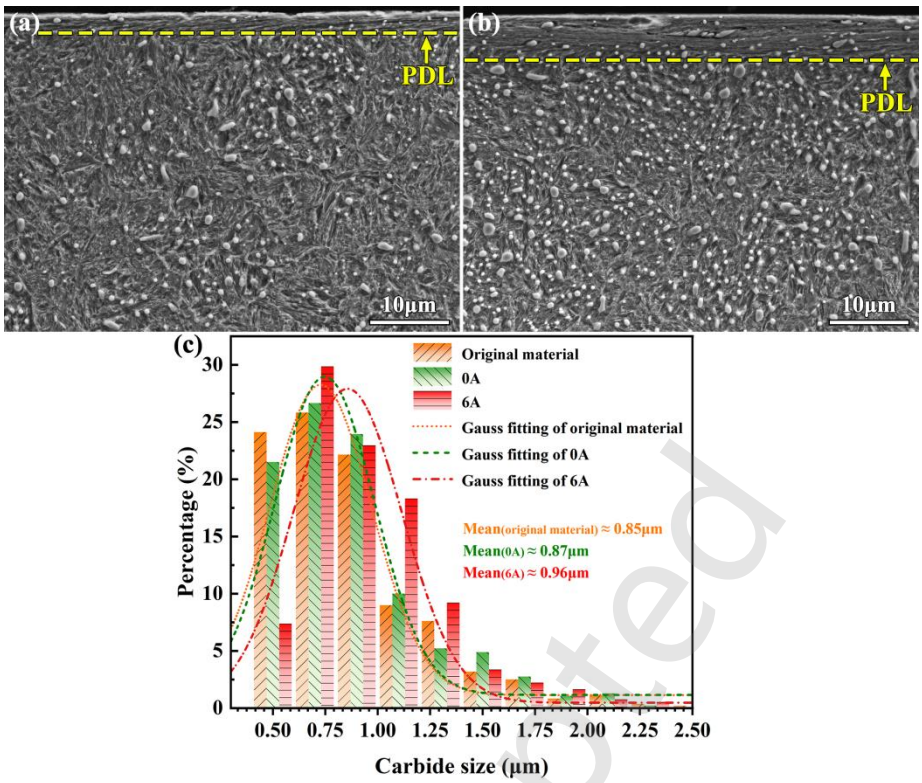

Fig. 14 (a) Subsurface SEM image of the wear track after 120 min of wear under 0 A; (b) Subsurface SEM image of the wear track after 120 min of wear under 6 A; (c) Statistical comparison of subsurface carbide sizes in the original material and after 120 min of wear under 0 A and 6 A conditions.

To investigate the influence of current-carrying wear on surface hardness, XRD was conducted to characterize the microstructure of the wear tracks under various conditions, as shown in Fig. 15. In Figs. 15(a-c), the disappearance of austenite peaks relative to the original material (Fig. 1(b)) indicates a transformation into martensite during wear. This stress-induced transformation can enhance surface hardness due to the higher hardness of martensite [62]. However, the contribution is limited by the low retained austenite content. To further assess microstructural changes, Gaussian fitting of the (100)α, (200)α, and (211)α diffraction peaks was conducted using Origin to obtain full width at half maximum (FWHM) and peak positions (2θ), as shown in Figs. 15(d-f). Compared with conventional wear, current-carrying wear leads to a significant increase in FWHM, which further broadens with increasing current. This typically reflects reduced grain size and increased microstrain [63, 64]. Elevated temperatures under current promote plastic shear and deformation, contributing to finer grains. According to the Hall-Petch relationship, decreasing grain size increases the strength of polycrystalline materials by introducing more grain boundaries that hinder dislocation motion [65]. Thus, the finer grains after current-carrying wear contribute to higher surface hardness compared to conventional wear. However, under 6 A, surface hardness did not continue

to increase with wear time and was even lower than that under 0 A at 120 min (Fig. 13(c)), indicating that factors beyond grain refinement also affect hardness evolution.

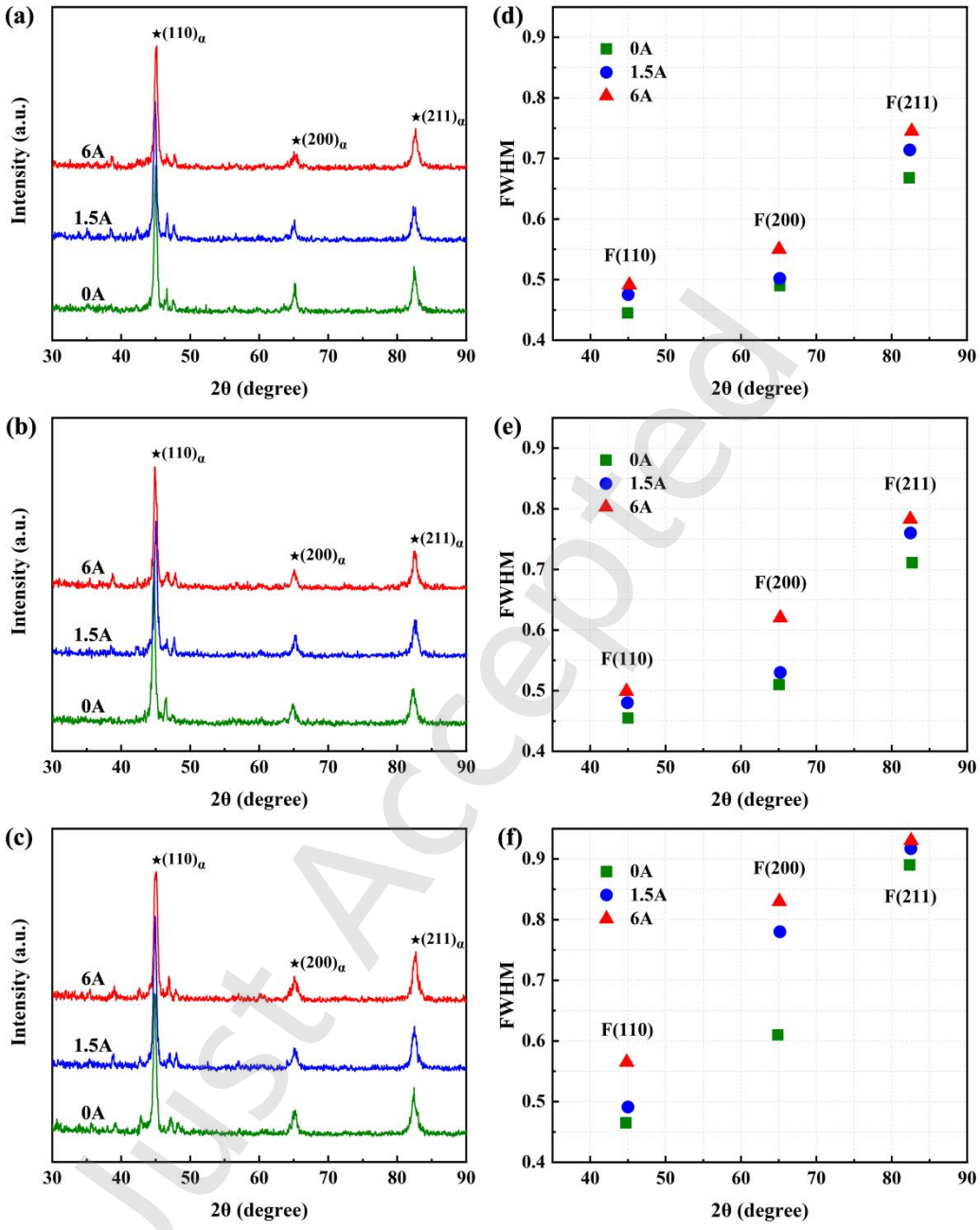

Fig. 15 XRD patterns and corresponding FWHM of wear tracks under different current levels and wear times: (a), (d) after 30 min of wear; (b), (e) after 60 min of wear; (c), (f) after 120 min of wear.

During prolonged plastic deformation, material strength is largely governed by dislocation interactions [66]. In metals such as copper and steel, grain size strengthening contributes only 10-12%, while dislocation strengthening accounts for 88-90% [67]. This aligns with the findings of Li et al. [68], who applied the LASSO method to analyze the hardness of cold-rolled steel and identified dislocation density as the dominant factor. The

dislocation density induced by plastic strain can be estimated using the Williamson-Hall (WH) method [69], described by:

$$\delta\cos\theta = \frac{K\lambda}{D} + 2\varepsilon\sin\theta \tag{4}$$

where θ is the diffraction angle, δ is the FWHM of the peak, K is the Scherrer constant (~0.9), λ is the Cu Kα wavelength (~0.154 nm), D is the grain size, and ε is the average microstrain. A linear fit of $\delta\cos\theta$ versus $2\sin\theta$ yields ε as the slope and $K\lambda/D$ as the intercept. Dislocation density is then calculated by [70]:

$$\rho = \frac{14.4\varepsilon^2}{b^2} \tag{5}$$

where b is the Burgers vector (~0.25 nm). Based on the XRD results in Fig. 15, dislocation densities under different wear conditions were calculated using the WH method, as shown in Fig. 16. Current-carrying wear resulted in notably higher dislocation densities than conventional wear at both 30 and 60 min. Under 6 A, values reached $6.12 \times 10^{14}\,m^{-2}$ and $9.12 \times 10^{14}\,m^{-2}$, approximately 1.4 and 1.3 times those under 0 A, respectively. At 120 min, dislocation densities at 0 A and 1.5 A were similar, with values of $3.15 \times 10^{15}\,m^{-2}$ and $3.34 \times 10^{15}\,m^{-2}$, respectively, while the 6 A condition showed a lower value of $1.88 \times 10^{15}\,m^{-2}$.

Under the 6 A condition, the lower dislocation density and more pronounced grain refinement after 120 min suggest the occurrence of dynamic recrystallization (DRX). As discussed in Section 4.1, the wear track temperature is conservatively estimated at 600 ℃. Although this is below the typical DRX initiation temperature for martensitic steels (approximately 750 ℃ [58]), transient local temperatures from arc discharge may exceed this threshold. Additionally, high dislocation density can provide sufficient strain energy to promote DRX at subcritical temperatures [71]. During DRX, dislocations are reduced through annihilation and grain boundary migration, resulting in the formation of finer recrystallized grains. Under cyclic loading, these grains remain stable and exhibit limited growth. In fact, DRX has been reported in current-assisted cutting of bearing steels and is considered a major factor in reducing work hardening [61]. In that study, the fractions of recrystallized and deformed grains increased from 9.23% and 14.82% under conventional cutting to 9.86% and 22.80% under a current density of 0.075 A/mm^2, while the grain size decreased from 1.103 μm to 0.777 μm.

In summary, surface hardness during current-carrying wear is influenced by multiple factors. In the early stage, elevated temperatures soften the matrix and increase plastic strain, while grain refinement and dislocation accumulation enhance hardness compared to conventional wear. With prolonged wear, tempering reduces matrix strength and weakens the hardened layer. Under 6 A, sustained high temperatures trigger DRX, leading to

dislocation annihilation. Despite grain refinement, the resulting decrease in dislocation density ultimately reduces surface hardness.

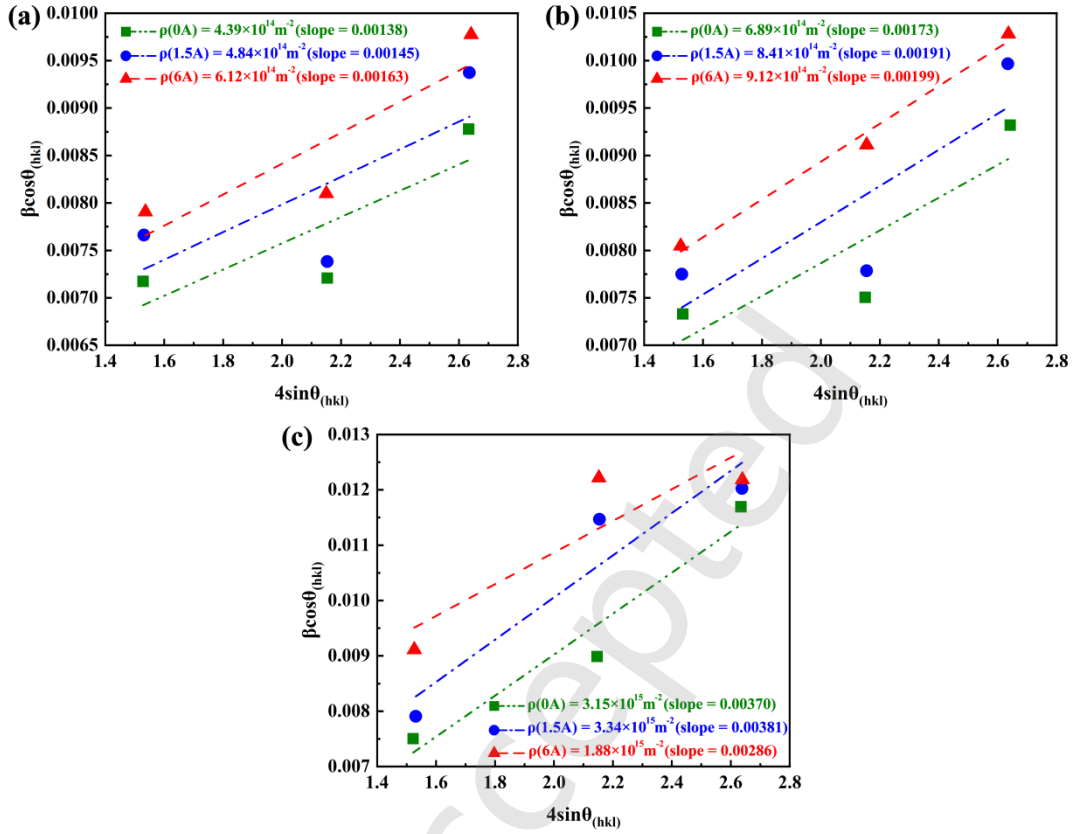

Fig. 16 Linear fitting results based on the WH method and corresponding dislocation densities (ρ(0 A), ρ(1.5 A), and ρ(6 A) represent the dislocation densities under currents of 0 A, 1.5 A, and 6 A, respectively): (a) after 30 min of wear; (b) after 60 min of wear; (c) after 120 min of wear.

4.4 Athermal effects of electric current on the mechanical properties of bearing steel

Plastic deformation in metals mainly occurs via dislocation slip. During current-carrying wear, elevated temperatures reduce the energy barrier for dislocation motion, while athermal effects of the electric current may also contribute to increased surface strain. Studies suggest that drifting electrons can interact with dislocations and transfer momentum, promoting their motion through the electron wind effect [72, 73]. Li et al. [74] used gold nanocrystals to model dislocations and found that drifting electrons increase atomic vibrations near dislocation cores, facilitating their migration. Qian et al. [75] observed current-induced dislocation motion in M50 steel via in situ TEM, and confirmed through DFT and MD simulations that this results from current-induced athermal effects enhancing atomic interactions in defect regions. In this study, plastic strain during wear led to high dislocation density in the subsurface. Athermal effects may accelerate dislocation rearrangement, relieve local pile-ups, and promote unpinning or climb, thereby enhancing dislocation mobility and plastic deformation.

The athermal effects of electric current on material plasticity have been widely demonstrated [76]. For example, pulsed current significantly improves the formability of aluminum alloys, where Joule heating is not the main softening mechanism [77]. Rudolf et al. [78] performed uniaxial tensile tests with constant DC current on polycrystalline copper, iron, and titanium, along with temperature-matched controls. Titanium exhibited the strongest athermal response, with a 20% reduction in tensile strength. Zhao et al. [79] found that electric pulses enhanced cross-slip in Ti-Al alloys, producing wavy dislocation structures similar to those in low-temperature deformation. They attributed this electroplastic behavior to defect-level microstructural reconstruction beyond the effects of Joule heating. The enhancement of plasticity by athermal effects can be interpreted through thermally activated dislocation motion, described by the Arrhenius equation [79]:

$$\dot{\gamma} = \dot{\gamma}_0 \exp\left[-\frac{\Delta H(\tau)}{KT}\right] \tag{6}$$

where $\dot{\gamma}$ is the shear strain rate, $\dot{\gamma}_0$ is the pre-exponential factor including mobile dislocation density and lattice vibration frequency, $\Delta H(\tau)$ is the activation enthalpy inversely related to the applied shear stress τ, K is the Boltzmann constant, and T is the temperature. Dislocation mobility can be enhanced by reducing activation enthalpy, increasing lattice vibration frequency, and raising temperature. In addition, the electric current force, defined as acting directionally on defect atoms, will increase the stress τ and thereby reduce $\Delta H(\tau)$.

Under the present conditions, it is difficult to isolate the athermal effects of electric current on plastic deformation at the worn surface, as thermal effects may dominate and mask weaker athermal contributions. However, Fig. 9 shows that the temperature measured 2 mm beneath the wear track remains relatively low across the tested current levels, and is generally insufficient to induce pronounced microstructural evolution or bulk mechanical-property changes in bearing steel. Considering heat conduction and dissipation through the specimen thickness, the thermal influence at the bottom of the specimen should be even weaker. Therefore, comparing post-wear mechanical-property changes in the bottom region across different currents may allow an indirect assessment of the possible contribution of athermal current effects under conditions of relatively weak thermal influence. To evaluate this, tensile specimens were extracted from the bottom of disk samples (~7 mm below the wear surface) worn for 60 and 120 min under different currents. The specimen preparation and dimensions are shown in Fig. 17(a). All tests were performed at a constant strain rate of 0.001 mm/s until fracture. Because each current level and wear duration was repeated three times, the corresponding tensile tests were also performed three times. The results are shown in Figs. 17(b-d). After current-carrying wear, the tensile strength of the bulk material decreased compared to the original sample. At 60 min, strengths under 1.5 A and 6 A were 1812.3 MPa and 1773.7 MPa, representing

reductions of 3.48% and 5.53% from the original 1877.6 MPa. This reduction became more pronounced at 120 min, with strengths dropping to 1770.4 MPa and 1733.3 MPa, corresponding to decreases of 5.71% and 7.69%, respectively. In contrast, conventional wear (0 A) caused no significant change. It should be noted that the strength change may be influenced by localized Joule heating arising from microscale electrical-resistance inhomogeneities. However, given the relatively uniform microstructure and good thermal conductivity of the present material (as discussed in Section 4.1), heat diffusion and homogenization are facilitated. Therefore, sustained and pronounced internal temperature gradients are unlikely to develop and significantly contribute to the strength changes. The consistent trends across repeated tests further indicate that the strength reduction is not an isolated outlier, thereby reducing the likelihood that localized Joule heating accounts for the observed differences. Taken together, the current-dependent decrease in bulk strength after current-carrying wear suggests a possible contribution from athermal effects.

Under current-carrying conditions, athermal effects not only promote dislocation motion but also encourage interactions like slip, cross-slip, and annihilation, leading to dislocation rearrangement [80]. As current and duration increase, dislocation interactions intensify, creating density gradients that weaken local strengthening, induce stress concentrations, and promote micro-defects. These factors can affect mechanical properties during plastic deformation. For example, Zhang et al. [21] reported a 24.4% drop in maximum flow stress and a 32.2% rise in reduction in area for M50 bearing steel under electrically assisted tension, attributed to athermal effects that enhance dislocation activity and weaken strain hardening. Wang et al. [22] proposed that electron wind may increase the local vacancy concentration, enhancing dislocation climb and slip activation and thereby lowering the critical resolved shear stress and deformation resistance in high-strength steels. Related studies also reported that athermal effects can promote localized recrystallization and reduce dislocation density in low-carbon steels, with stronger effects at higher current densities [17]. In addition, Gould et al. [81] reported that AISI 52100 bearings under electrical conditions were more prone to white etching cracks, attributed to localized plasticity from dislocation-current interactions. Overall, these studies suggest that the bulk strength reduction observed after current carrying-wear in this study may be linked to athermal effects induced by electric current through defect evolution and the associated changes in mechanical response. However, this remains a hypothesis, as mechanical testing alone cannot fully confirm athermal effects. Further microstructural analysis will be needed for validation, which will be addressed in future work. In summary, subsurface shear strain in current-carrying wear is primarily driven by thermal effects, with athermal effects acting as a secondary contributor, together influencing both mechanical properties and tribological behavior.

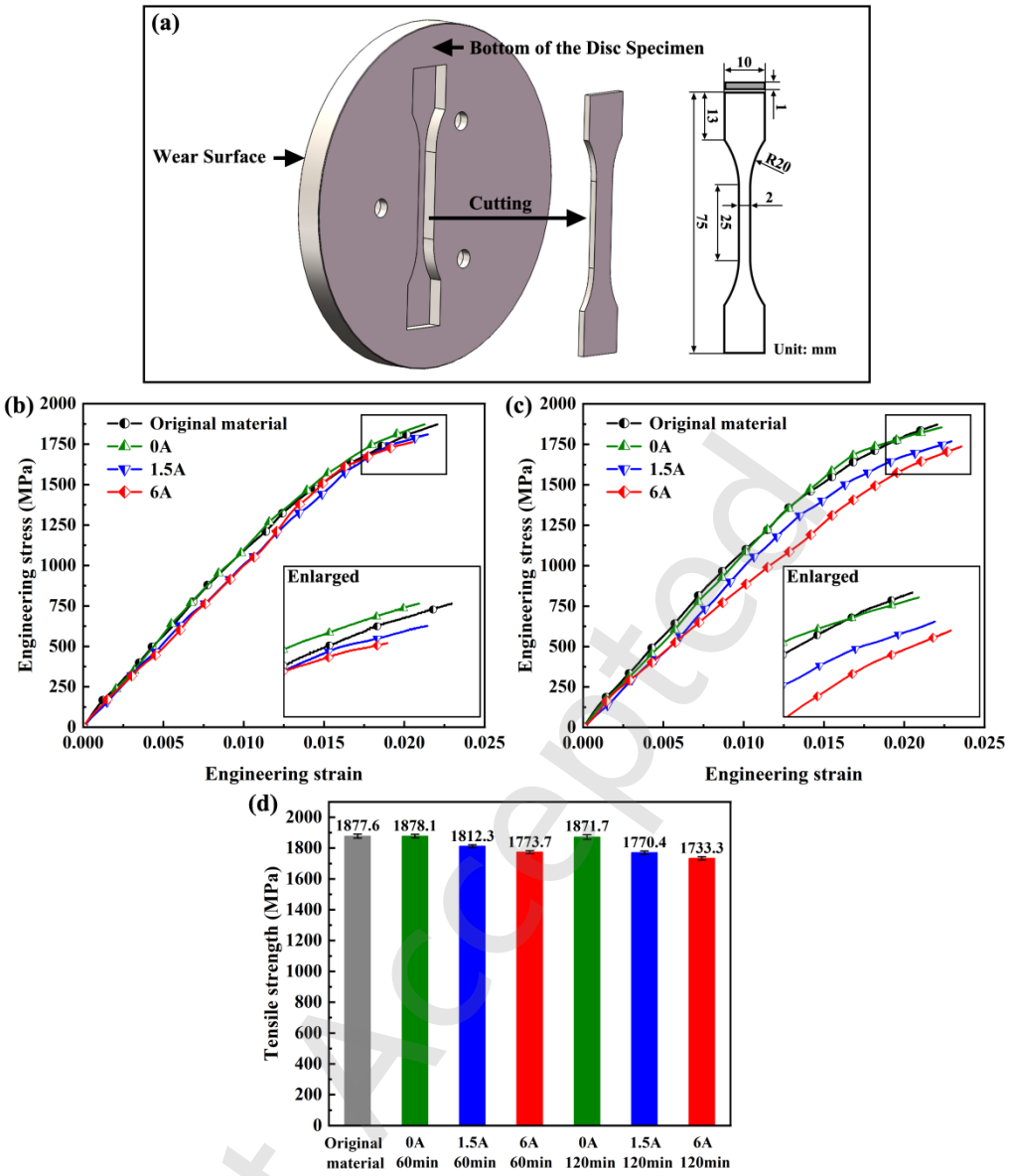

Fig. 17 (a) Schematic diagram of specimen preparation and dimensions for tensile testing; (b) tensile test results comparing the bulk material after 60 min of wear under different current levels with the original material; (c) tensile test results comparing the bulk material after 120 min of wear under different current levels with the original material; (d) tensile strength statistics for all tensile tests.

5 Conclusion

In this study, sliding wear tests were conducted on AISI 52100 bearing steel under oil-lubricated conditions with varying electric currents and wear times to investigate the effect of electric current on its tribological behavior and associated microstructural degradation mechanisms. The main conclusions are as follows:

(1) Under current-carrying conditions, arc discharge in conjunction with frictional heating significantly raises the wear temperature. While the early-stage temperature rise is comparable to the no-current case at low currents,

prolonged wear leads to increased arc activity and a rapid temperature escalation within the wear track.

(2) Electric current induces a fundamental shift in wear mechanisms. In the absence of current, abrasive wear prevails with mild oxidation over time. Conversely, current-carrying conditions cause severe oxidative, abrasive, and adhesive wear from the early stages, resulting in elevated coefficient of friction and wear volume.

(3) High interfacial temperatures during current-carrying wear trigger tempering and dynamic recrystallization in the subsurface, softening the microstructure and promoting plastic deformation. These thermal effects facilitate microcrack initiation and may accelerate fatigue failure.

(4) Athermal effects of electric current enhance dislocation motion and facilitate structural rearrangement, which progressively degrade the mechanical properties of bearing steel with increasing current and exposure time, ultimately impairing its tribological performance.

Overall, our results indicate that the current-carrying degradation of bearing steel is primarily driven by arc-discharge-induced localized overheating. Under 6 A (~36 A/mm^2), the wear surface temperature may reach on the order of 300 ℃ after 30 min. This suggests that suppressing arc discharge and keeping the current density as low as practicable should be prioritized to mitigate friction and wear degradation. Practical measures include interfacial insulation (insulated bearings/coatings) and sufficient lubrication to maintain a continuous film and improve electrical insulation. In addition, after 120 min of wear, the bulk tensile strength decreased by approximately 5.71% and 7.69% under 1.5 A (~9 A/mm^2) and 6 A, respectively, indicating that electric current may also affect mechanical properties through athermal effects. Correspondingly, appropriate heat treatment or surface modification can be used to enhance material stability and near-surface strength, thereby alleviating these potential adverse effects and reducing possible long-term reliability risks.

Acknowledgements

This work was financially supported by Natural Science Foundation of China NSFC (No. 52575183), Strategic Priority Research Program of the Chinese Academy of Sciences (No. XDB1210000), Ningbo Key Technologies R & D Program (2025Z006), 2024 Key R&D Project of Cixi, Ningbo (CZ2025012) and K.C. Wong Magna Fund in Ningbo University.

Declaration of competing interest

The authors have no competing interests to declare that are relevant to the content of this article.

References

[1] Niu K, Song C F, Lou Z H, Pang X J, Lu H H, Du S M, Zhang Y Z. Electric damage of bearing under AC shaft voltage at different rotation speeds. Tribol Int 177: 108008 (2023)

[2] Esmaeili K, Wang L, Harvey T J, White N M, Holweger W. Electrical discharges in oil-lubricated rolling contacts and their detectionusing electrostatic sensing technique. Sensors 22(1): 392 (2022)

[3] He F, Xie G X, Luo J B. Electrical bearing failures in electric vehicles. Friction 8(1): 4-28 (2020)

[4] Farfan-Cabrera L I. Tribology of electric vehicles: A review of critical components, current state and future improvement trends. Tribol Int 138: 473-486 (2019)

[5] Spikes H A. Triboelectrochemistry: Influence of applied electrical potentials on friction and wear of lubricated contacts. Tribol Lett 68(3): 90 (2020)

[6] Farfan-Cabrera L I, Erdemir A, Cao-Romero-Gallegos J A, Alam I, Lee S. Electrification effects on dry and lubricated sliding wear of bearing steel interfaces. Wear 516: 204592 (2023)

[7] Hsu S, Ying C, Zhao F. The nature of friction: A critical assessment. Friction 2(1): 1-26 (2014)

[8] Ma J J, Xue Y J, Han Q K, Li X J, Yu C X. Motor bearing damage induced by bearing current: A review. Machines 10: 1167 (2022)

[9] Song C F, Ren Y L, Huang Q R, Zhang Y Y, Li Y H, Cheng J H, Pang X J, Zhang Y Z. Effect of shaft voltage on electric damage of GCr15 bearing material. Tribol Int 200: 110139 (2024)

[10] Didenko T, Pridemore W D. Electrical fluting failure of a Tri-lobe roller bearing. J Fail Anal Prev 12: 575-580 (2012)

[11] Cai Z B, Li C L, You L, Chen X D, He L P, Cao Z Q, Zhang Z N. Prediction of contact resistance of electrical contact wear using different machine learning algorithms. Friction 12(6): 1250-1271 (2024)

[12] Wu H H, Liu C S, Niu G Q, Zhang L, Liu H Q, Kang X. Effect of the contact load and rotation speed on the formation of rolling current-carrying arc and the corresponding material damage. J Mater Res Technol 23: 1696-1703 (2024)

[13] Xue P D, Chen C, Fan X, Diao D F. Current-carrying friction in carbon coated ball bearing. Friction 11(11): 2008-2020 (2023)

[14] Jeong H J, Park J W, Shin E, Woo W, Kim M J, Han H N. Electric current-induced precipitation hardening in advanced high-strength steel. Scr Mater 220: 114933 (2022)

[15] Kim M J, Lee K, Oh K H, Choi I S, Yu H H, Hong S T, Han H N. Electric current-induced annealing during uniaxial tension of aluminum alloy. Scr Mater 75(15): 58-61 (2014)

[16] Kim M J, Lee M G, Hariharan K, Hong S T, Choi I S, Kim D, Oh K H, Han H N. Electric current-assisted deformation behavior of Al-Mg-Si alloy under uniaxial tension. Int J Plast 94: 148-170 (2017)

[17] Jeong K, Jin S W, Kang S G, Park J W, Jeong H J, Hong S T, Cho S H, Kim M J, Han H N. Athermally enhanced recrystallization kinetics of ultra-low carbon steel via electric current treatment. Acta Mater 232: 117925 (2022)

[18] Xiang S Q, Zhang X F. Dislocation structure evolution under electroplastic effect. Mater Sci Eng A 761: 138026 (2019)

[19] Molotskii M, Fleurov V. Magnetic effects in electroplasticity of metals. Phys Rev B 52(22): 15829-15834 (1995)

[20] Okazaki K, Kagawa M, Conrad H. An evaluation of the contributions of skin, pinch and heating effects to the electroplastic effect in titatnium. Mater Sci Eng 45(2): 109-116 (1980)

[21] Zhang Z C, Wang F, Yin F, Qian D S, Liu X Y, Wu M. Microstructure evolution and deformation behaviors of pulse electro-assisted deformation in M50 bearing steel. J Mater Res Technol 23: 4909-4921 (2023)

[22] Wang Y, Deng T Q, Chang X S, Qi Y S, Chen G, Chen Q. High temperature electropalsticity in Aermet100 steel by decoupling electron wind effect. Mater Sci Eng A 915: 147293 (2024)

[23] Cao-Romero-Gallegos J A, Farfan-Cabrera L I, Erdemir A, Pascual-Francisco J B. Lubricated sliding wear of gear material under electrification - A new approach to understanding of the influence of shaft currents in the wear of EV transmissions. Wear 523: 204782 (2023)

[24] Safdarzadeh O, Farahi A, Binder A, Sezen H, Hofmann J P. WLI, XPS and SEM/FIB/EDS surface characterization of an electrically fluted bearing raceway. Lubricants 12(148): 12050148 (2024)

[25] Ye H, Yin J, Wang X B, Lou W J, Liang P, Liu H C. Electrical fluting damage of rolling element bearings: Influences of AC electrical parameters and operating conditions. Tribol Int 208: 110658 (2025)

[26] Yang Z H, Song Y J, Jiao J L, Li W B, Bao S G, Zhang Y Z. Optimization of current-carrying friction and wear properties of copper-carbon composite materials based on damage. Tribol Int 191: 109074 (2024)

[27] Grandin M, Wiklund U. Wear phenomena and tribofilm formation of copper/copper-graphite sliding electrical contact materials. Wear 398-399: 227-235 (2018)

[28] Kapoor R, Nemat-Nasser S. Determination of temperature rise during high strain rate deformation. Mech Mater 27(1): 1-12 (1998)

[29] Rigney D A, Karthikeyan S. The evolution of tribomaterial during sliding: A brief introduction. Tribol Lett 39: 3-7 (2010)

[30] Zhai W Z, Shi X L, Xu Z S, Zhang A. Investigation of the friction layer of Ni_3Al matrix composites. Wear 328-329: 39-49 (2015)

[31] Rupert T J, Schuh C A. Sliding wear of nanocrystalline Ni-W: structural evolution and the apparent breakdown of archard scaling. Acta Mater 58: 4137-4148 (2010)

[32] Kim M J, Bui-Thi T A, Kang S G, Hong S T, Han H N. Electric current-induced phenomena in metallic materials. Curr Opin Solid State Mater Sci 32: 101190 (2024)

[33] Scepanskis M, Jakovics A, Kaldre I, Holweger W, Nacke B, Diederichs A M. The numerical model of electrothermal deformations of carbides in bearing steel as the possible cause of white etching cracks initiation. Tribol Lett 59: 37 (2015)

[34] Zhao H, Feng Y, Zhou Z J, Qian G, Zhang J C, Huang X C, Zhang X B. Effect of electrical current density, apparent contact pressure, and sliding velocity on the electrical sliding wear behavior of Cu-Ti_3AlC_2 composites. Wear 444-445: 203156 (2020)

[35] Ashraf Y K, Javeed S, Zeeshan S, Khalid R, Janjua SA, Ahmad S. Sublimation of graphite in continuous and pulsed arc discharges. Turk J Phys 34: 33-42 (2010)

[36] Huang D L, Xiao J K, Wang C, Zhang Z Z, Chen J, Li A K, Zhang C. Tribological property of AgNi-CNTs composites under electric current. Wear 564-565: 205712 (2025)

[37] Sakai T, Belyakov A, Kaibyshev R, Miura H, Jonas J J. Dynamic and post-dynamic recrystallization under hot, cold and severe plastic deformation conditions. Prog Mater Sci 60: 130-207 (2014)

[38] Kano R, Nemoto Y, Maeda Y, Yamamoto S, Iwao T. Arc temperature measurement with microsecond spectroscopic measurement. Electr Eng Jpn 210: 29-36 (2020)

[39] Liu X L, Hu M J, Li Z H, Zhou C W, Xiao Q, Yang W B, Chen D Y. Effect of copper contents on the current-carrying wear properties of carbon brush under different temperatures conditions. J Mater Res Technol 15: 3110-3121 (2021)

[40] Deshpande P, Yelkarasi C, Lee S, Farfan-Cabrera L I, Erdemir A. Electrotribochemical formation of abrasive nano-carbon particles under electrified conditions on lubricated sliding contacts. Carbon 228: 119425 (2024)

[41] Testa-Anta M, Ramos-Docampo M A, Comesana-Hermo M, Rivas-Murias B, Salgueirino V. Raman spectroscopy to unravel the magnetic properties of iron oxide nanocrystals for bio-related applications. Nano Adv 1: 2086-2103 (2019)

[42] Chen D, Zhang P, Deng Q, Deng M J, Yue Z W, Cai Z B, Gu L. Comparative investigation on the fretting and sliding wear properties of TC4 against GCr15 under different temperatures. Tribol Int 199: 109980 (2024)

[43] Wei P, Bai P P, Yue L, Zhou X, Wen X L, Zhao H, Tian Y. Comparing friction behavior and mechanism of three generation bearing steel (GCr15, M50, CSS-42L) paired silicon nitride under ester oil lubrication from room temperature to 350 ℃. J Mater Res Technol 30: 1354-1367 (2024)

[44] Ruiz-Andres M, Conde A, Damborenea J, Garcia I. Friction and wear behaviour of dual phase steels in discontinuous sliding contact conditions as a function of sliding speed and contact frequency. Tribol Int 90: 32-42 (2015)

[45] Kim K J, Moon D W, Lee S K, Jung K H. Formation of a highly oriented FeO thin film by phase transition of Fe_3O_4 and Fe nanocrystallines. Thin Solid Films 360: 118-121 (2000)

[46] Lawless K R. The oxidation of metals. Rep Prog Phys 37: 231 (1974)

[47] Yang R, Guo X, Yang H J, Qiao J W. Tribological behavior of boronized Fe40Mn20Cr20Ni20 high-entropy alloys in high temperature. Surf Coat Technol 464: 129572 (2023)

[48] Wang P, Wu K W, Wu W C, Pan A, Guo Z M, Chen S L. Current-carrying wear behavior of $CoCrFeNiW_{0.2}$ and $CoCrFeNiW_{0.2}$+3at%C high entropy alloys. Tribol Int 197: 109749 (2024)

[49] Tong Y L, Zhang T Y, Zhang S H. Influence of oxides on the formation of self-lubricating layer and anti-wear performance during sliding. Tribol Int 179: 108188 (2023)

[50] Yu Z Q, Yang Z G. Fatigue failure analysis of a grease-lubricated roller bearing from an Electric Motor. J Fail Anal Prev 11(2): 158-66 (2011)

[51] Romanenko A, Muetze A, Ahola J. Effects of electrostatic discharges on bearing grease dielectric strength and composition. IEEE Trans Ind Appl 52(6): 4835-4842 (2016)

[52] Xie G X, Luo J B, Liu S H, Guo D, Zhang C H, Si L N. Electrospreading of dielectric liquid menisci on the small scale. Soft Matter 7(13): 6076-6081 (2011)

[53] Yang H M, Li J S, Zeng X Q. Tribological behavior of nanocarbon materials with different dimensions in aqueous systems. Friction 1(16): 29-46 (2020)

[54] Xie G X, Luo J B, Liu S H, Zhang C H, Lu X C. Micro-bubble phenomenon in nanoscale water-based lubricating film induced by external electric field. Tribol Lett 29(3): 169-176 (2008)

[55] Hurricks P L. The effect of applied voltage on the frictional behaviour of carbon black filled elastomers. Wear 52(2): 365-380 (1979)

[56] Cao-Romero-Gallegos J A, Taghizadeh S, Aguilar-Rosas O A, Dwyer-Joyce R S, Farfan-Cabrera L I. The effect of electrical current on lubricant film thickness in boundary and mixed lubrication contacts measured with ultrasound. Friction 12(8):1882-1896 (2024)

[57] Liu X C, Zhang H W, Lu K. Formation of nano-laminated structure in nickel by means of surface mechanical grinding treatment. Acta Mater 96: 24-36 (2015)

[58] Su Y S, Li S X, Gao Q Y, Jiang H, Lu S Y, Yu F, Shu X D. Evolution of nano-laminated structure formed by the thermally-assisted plastic deformation in dry sliding wear. Tribol Int 140: 1005846 (2019)

[59] Yin C H, Liang Y L, Liang Y, Li W, Yang M. Formation of a self-lubricating layer by oxidation and solid-state amorphization of nano-lamellar microstructures during dry sliding wear tests. Acta Mater 166: 208-220 (2019)

[60] Kapoor A, Franklin F J. Tribological layers and the wear of ductile materials. Wear 245(1-2): 204-215 (2000)

[61] Sun F J, Yi J H, Liang Z Q, Lu Y J, Chen J L, Xiao G, Li X Z, Xiao Y B, Huang H, Yuan J P. Enhancement of machinability and surface tribological property of hardened bearing steel by electric pulse-assisted hard turning. Tribol Int 199: 110022 (2024)

[62] Yang Z N, Ji Y L, Zhang F C, Zhang M, Nawaz B, Zheng CL. Microstructural evolution and performance change of a carburized nanostructured bainitic bearing steel during rolling contact fatigue process. Mater Sci Eng A 725: 98-107 (2018)

[63] Nie M H, Jiang P F, Li X R, Zhu D D, Yue T L, Zhang Z H. Directed energy deposition combined with interlayer remelting for improving NiTi wear resistance by grain refinement. Tribol Int 202:110300 (2025)

[64] Das-Bakshi S, Sinha D, Ghosh-Chowdhury S. Anisotropic broadening of XRD peaks of α′-Fe: Williamson-Hall and Warren-Averbach analysis using full width at half maximum (FWHM) and integral breadth (IB). Mater Charact 142: 144-153 (2018)

[65] Hu Y, Zhou L, Ding H H, Lewis R, Liu Q Y, Guo J, Wang W J. Microstructure evolution of railway pearlitic wheel steels under rolling-sliding contact loading. Tribol Int 154: 106685 (2021)

[66] Zhao Y H, Liao X Z, Jin Z, Valiev R Z, Zhu Y T. Microstructures and mechanical properties of ultrafine grained 7075 Al alloy processed by ECAP and their evolutions during annealing. Acta Mater 52(15): 4589-4599 (2004)

[67] Costa A L, Reis A C, Kestens L, Andrade M S. Ultra grain refinement and hardening of IF-steel during accumulative roll-bonding. Mater Sci Eng A 406(1-2): 279-285 (2005)

[68] Li W, Vittorietti M, Jongbloed G, Sietsma J. The combined influence of grain size distribution and dislocation density on hardness of interstitial free steel. J Mater Sci Technol 45: 35-43 (2020)

[69] Izuta Y, Prasad K, Ito A, Tanaka M, Torizuka S. Transmission X ray diffraction characterization of deformation induced martensite in 301 and 304 stainless steels rolled at 77K: Role of grain size. Mater Sci Eng A 794: 139984 (2020)

[70] Zhou P W, Yang W L, Wu Y C, Zong Y Y. Characterization of microstructural evolution with pre-strain in BG801 bearing steel: Grain, carbides, retained austenite and martensite. Vacuum 216: 112354 (2023)

[71] Nagashima F, Nakagawa Y, Yoshino M. Influence of severe plastic deformation on static recrystallization microstructure of pure iron. Metals 10(10): 1320 (2020)

[72] Troitskii O A. Electroplastic deformation of metals. Strength Mater 8: 1466-1471 (1976)

[73] Wang X W, Xu J, Jiang Z L, Zhu W L, Shan D B, Guo B, Cao J. Size effects on flow stress behavior during electrically-assisted micro-tension in a magnesium alloy AZ31. Mater Sci Eng A 659: 215-224 (2016)

[74] Li X, Zhu Q, Hong Y R, Zheng H, Wang J, Wang J W, Zhang Z. Revealing the pulse-induced electroplasticity by decoupling electron wind force. Nat Commun 13: 6503 (2022)

[75] Qian D S, Chen J C, Luo H, Wang F, Hua L. Electric current-induced directional slip of dislocation and grain boundary ordering. Mater Today Adv 24: 100530 (2024)

[76] Xu Z T, Jiang T H, Huang J H, Peng L F, Lai X M, Fu M W. Electroplasticity in electrically-assisted forming: Process phenomena, performances and modelling. Int J Mach Tools Manuf 175 :103871 (2022)

[77] Roh J H, Seo J J, Hong S T, Kim M J, Han H N, Roth J T. The mechanical behavior of 5052-H32 aluminum alloys under a pulsed electric current. Int J Plast 58: 84-99 (2014)

[78] Rudolf C, Goswami R, Kang W, Thomas J. Effects of electric current on the plastic deformation behavior of pure copper, iron, and titanium. Acta Mater 209: 116776 (2021)

[79] Zhao S T, Zhang R P, Chong Y, Li X Q, Abu-Odeh A, Rothchild E, Chrzan D C, Asta M, Morris J W, Minor A M. Defect reconfiguration in a Ti-Al alloy via electroplasticity. Nat Mater 20: 468-472 (2021)

[80] Song X D, Wang F, Qian D S, Hua L. Tailoring the residual stress and mechanical properties by electroshocking treatment in cold rolled M50 steel. Mater Sci Eng A 780: 139171 (2020)

[81] Gould B, Demas N, Erck R, Lorenzo-Martin M C, Ajayi O, Greco A. The effect of electrical current on premature failures and microstructural degradation in bearing steel. Int J Fatigue 145: 106078 (2020)